CIS II Final Report
In Situ Needle Path Adjustment and Trajectory Optimization

Yanzhou Wang

May 1, 2022

1 Introduction

Low back pain is an extremely common condition that has a huge economic impact; yet despite its prevalence,the actual source of pain is often times difficult to diagnose, and many different treatment methods have been proven effective to various degrees. Lumbar injection is among themostcommon tools to diagnose and treat low back pain, and typical targets ofinjection include the facet joint, sacroiliac joint, and the epidural space. These procedures are commonly performed under X-ray and fluoroscopy guidance, which inevitably exposes both the clinician and patient to ionizing radiation.

Image guided needle insertion with robot assistance is a research area that has amassed huge interest in the past two decaes, since robots have higher motion accuracy and repeatability,and are not affected by radiation. However, although many teams have demonstrated great targeting accuracy with flexible needles in a lab environment, few have implemented these methods in actual products; as far as we are aware, all commercialized needle insertion robots have a manual operation mode, where the actual insertion step is still performed by the clinician themself. It is a diverse field that involves a numher of different subject areas, such asrobot system design, soft tissue and needle modeling, path planning, and control.

During an actual procedure, when the clinician detects an error in needle placement, they can quickly gather their prior experience and utilize the reaction force from the needle to make small, yet effective, adjustment at the needle base. These fine finger and hand motions, coupled with intermediate imaging, help the clinician to guide the needle closer and closer to the actual target. One of the main goals for this project is to examine this adjustment process in greater detail, and enable future robotic systems to make such adjustments while the needle is still inserted into the tissue, correcting the needle from its deviated path [5].

2 Methods

To properly study this needle adjustment motion and its effect on the flexible needle and soft tissue, a test jig needs to be build to replicate, and allow for detection of, such motion via some imaging techniques. A needle-tissue interaction model is proposed based on Euler-Bernouli beam theory and biomechanics, and solved via nonlinear finite element method; the validity of such model needs to be tested with the jig. Finally, with such interaction model in place, its extension to boundary control problem will be briefly examined, which will be of great importance for optimal trajectory generation and tracking.

2.1 Test Jig, Image Registration, and Motion Extraction

To study the interaction between needle and soft tissue, (semi-)transparent tissue phantoms made out of liquid PVC are commonly used. Specific direction for making these samples is discussed in Appendix A In order to detect the shape of flexible needles inserted into these gel phantoms, the research community often relies on 2-D or 3-D cameras, with the assumption that the deformation of such gel is small enough that light diffraction can be ignored. This is not the case in the current situation, since needle bending will cause significant deformation of the tissue phantom, and light-based approaches cannot be used. In addition, needle shape cannot be detected by such approach when actual tissues are used, thus further diminishing the value of such approach.

To circumvent this issue, cone-beam CT is used as the imaging technique, and a test jig, shown in Figure 1, is built to replicate needle bending, and to allow motion extraction from CT volumes.

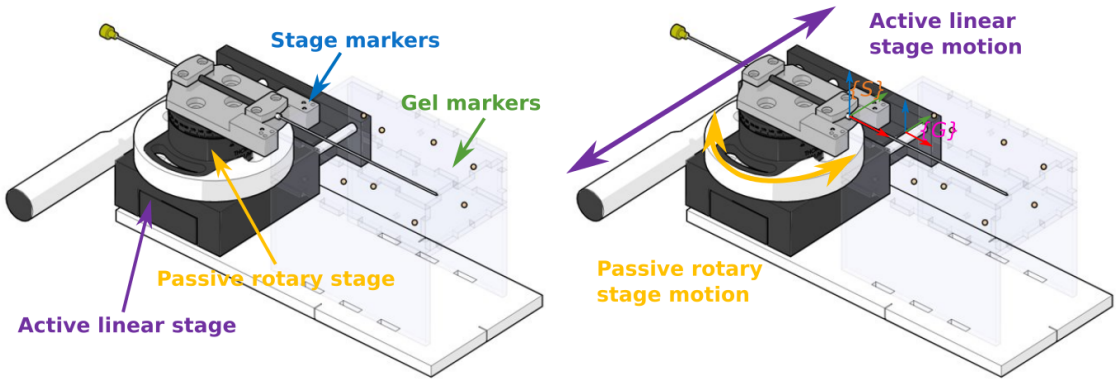

(a) Test jig design. (b) Test jig motion.

Figure 1: Test jig to replicate and allow motion capture of needle bending motion.

The jig includes an active linear stage, a passive rotary stage, steel markers on the needle holder stage (frame $\{S\}$) and gel container box (frame $\{G\}$). The needle goes through the stage and inserts into the medium held in the container. The gel markers are slightly larger than the stage markers so as to differentiate them in CT volumes. The scanning volume for the cone-beam CT is approximately $120 \times 120 \times 120\text{mm}^3$, and the components of the jig are positioned such that only parts that are useful for image registraion and motion extraction are included in the volume. A crosshair is cut on the acrylic base to position the jig relative to the C-arm, and to ensure no extra components enter the volume.

An active lateral translation will results in passive rotation of the rotary stage due to interaction between needle and medium. The net motion can be detected by subsequent transformations between frame $\{S\}$ and $\{G\}$ since $\{G\}$ remains stationary, provided that an initial transformation between the two frames are given prior to any motion. The relative position and orientation between the two frames can be determined from CT volumes as shown in Algorithm 1:

Algorithm 1 Relative frame transformation from CT

$CT\_Vol \leftarrow$ read CT volume
$[needle, gelMarker, stageMarker] \leftarrow$ CT segmentation ▷ based on sizes of connected components
Ensure: numbers in $gelMarker$ and $stageMarker$ agree with CAD
$GelF_{design}^{CT} \leftarrow icp(gelMarkerDesign, gelMarker)$ ▷ Gel frame serve as global origin
$CT\_Vol' \leftarrow applyTransform(GelF_{design}^{CT})$ ▷ Transform entire volume
$StageF_{CT}^{design} \leftarrow icp(stageMarker', stageMarkerDesign)$ ▷ Stage frame as moving frame
$[Rs, ts] \leftarrow$ Extract translation and rotation from $StageF_{CT}^{design}$

Since $\{G\}$ is taken as the global reference frame, each $\{S\}$ represents a moved configuration, and can be compared with $\{S_0\}$ obtained from a baseline volume to get motion parameters, particularly the lateral motion and rotation which are necessar inputs for the proposed needle-tissue interaction model.

2.2 Needle-Tissue Interaction and Biomechanical Model

The proposed needle-tissue interaction model resembles closely to Euler-Bernouli beam with flexible support. A free-body diagram of the physical scenario is shown in Figure 2. The needle, modeled as a homogeneous beam, is initially resting along the horizontal $x-$axis and embedded in multi-layer media. Boundary condition is applied to the free end of the needle such that the needle base is displaced in the positive direction by d_b, and tilted with a slope k_b. The free end is some s_b away from the point of insertion, and the total length embedded in the media is l. Due to the flexibility of the needle and the contact with

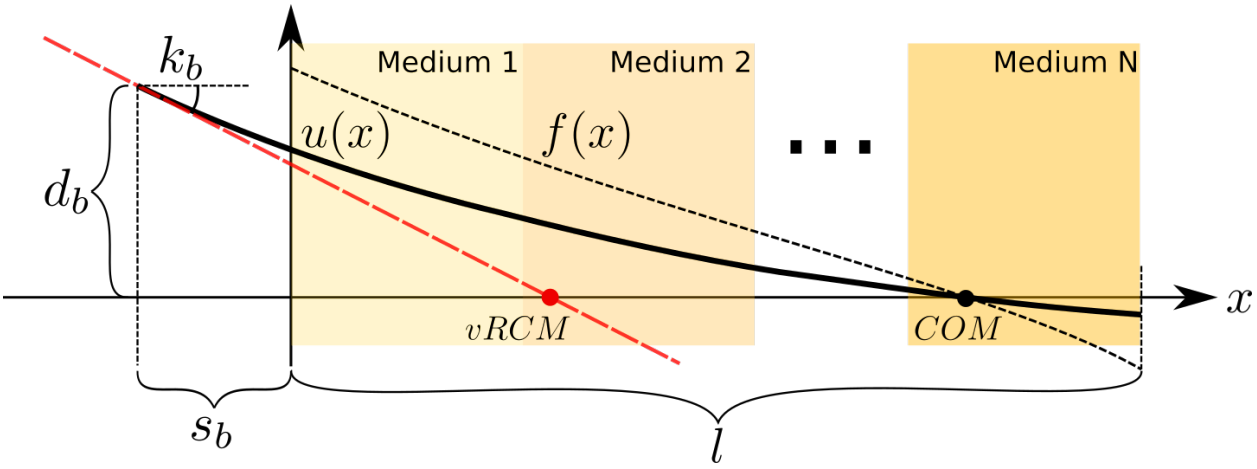

Figure 2: Needle-tissue interaction model schematic.

soft tissue, the needle will deform upon such deflection, assuming a shape function $u(x)$ ($x \in [-sb, l]$), and the corresponding force generated within the media is $f(x)$ ($x \in [0, l]$). If the media presents no resistance to the needle, the needle would intersect the $x-$axis at a virtual remote center of motion ($vRCM$) given a slope k_b; however, because the media will generate reaction force, the flexible needle will instead intersect the $x-$axis somewhere deeper, called the neeldle center of motion (COM).

The reaction force from the media, $f(x)$, will be somewhat proportional to the amount of compression, but the proportionality is dependent on the specific medium. To this end, considering some small frictional constants γ_T for each media T, the force is formulated as

$$f(x) = k(x)u(x)\left\{1 - \gamma_T \sin^2\left[\tan^{-1}(u_{,x}(x))\right]\right\}\mathcal{H}(x) \tag{1}$$

The Heaviside function $\mathcal{H}(x)$ is only used to switch between different media, and can be replaced with a lookup table in actual implementation. The constants γ_T is expected to contribute little to the force term, since the amount of relative motion along the longitudinal direction of the needle is small, so the term is only included for the sake of completeness. The notation $u_{,x}$ is a short hand notation for first derivative of $u(x)$ with respect to x.

Many literature on needle insertion modeling takes $k(x)$ as a constant k, and is compared with the Young's modulus E of the medium (or Winkler modulus K in civil engineering literature), assuming the compression is small enough that the stress-strain behavior resides in its linear range. This is not the case in the current scenario, since the deflection is significantly larger; many rubber-like materials and also soft tissues exhibit highly nonlinear behavior, so a constant parameter is unlikely to model the behavior well.

The function $k(x)$ will instead be given by the tangent modulus of the stress-stretch curve for one-term Ogden hyperelastic material model. The specific reason for choosing this hyperelastic material model will be explained Section 3.2.

The form of one-term Ogden hyperelastic material model is presented in Equation 2.

$$W = \frac{2\mu}{\alpha^2}(\lambda_1^\alpha + \lambda_2^\alpha + \lambda_3^\alpha - 3) - \rho(J-1) \tag{2}$$

where λ_1, λ_2, and λ_3 are the principal stretches; $J = \lambda_1\lambda_2\lambda_3$, and $J = 1$ is required by incompressibility, which is added to the strain energy density function by means of a Lagrange multiplier ρ. Here, we make the assumption that in a multilayer media, layer boundaries remain unchaged during needle motion, which leads to the deformation gradient

$$\mathbf{F} = \begin{bmatrix} \lambda_1 & 0 & 0 \\ 0 & \lambda_2 & 0 \\ 0 & 0 & \lambda_3 \end{bmatrix} = \begin{bmatrix} 1 & 0 & 0 \\ 0 & \lambda & 0 \\ 0 & 0 & \frac{1}{\lambda} \end{bmatrix} \tag{3}$$

if the primary stretch direction is in e_2 and the compression is constrained in e_1 but the material is free to expand in e_3.

Cauchy stress tensor can be calculated as

$$\sigma = \sum_{i=1}^{3} (\lambda_i \frac{\partial W}{\partial \lambda_i} - \rho) v^{(i)} \otimes v^{(i)} \tag{4}$$

with the assumption that the material is free to expand in e_3, $\sigma_{33} = 0 = \frac{2\mu}{\alpha}\lambda^{-\alpha} - \rho$, which leads to the solution of the Lagrange multiplier $\rho = \frac{2\mu}{\alpha}\lambda^{-\alpha}$. Thus the stress in primary compression direciton $\sigma_{22} = \frac{2\mu}{\alpha}(\lambda^{\alpha} - \lambda^{-\alpha})$, and the tangent modulus is calculated as

$$k(x) = \frac{\partial \sigma_{22}}{\partial \lambda} = 2\mu \left(\lambda^{\alpha-1} + \lambda^{-\alpha-1}\right) \quad \lambda = \frac{t_i - |u(x)|}{t_i} \tag{5}$$

where t_i is the initial length of the medium, and $u(x)$ is the displacement. Since the needle can only apply compression to the media, the absolute sign is used.

The complete form of the nonlinear equation is then formulated as follows (*Strong Form (S)*):

Given constants d_b and k_b, and function $f(x)$, find $u(x) \in C^4(-s_b, l)$ such that

$$EIu_{,xxxx} = f(x) \quad x \in (-s_b, l) \tag{6}$$
$$u(-s_b) = d_b \tag{7}$$
$$u_{,x}(-s_b) = k_b \tag{8}$$
$$u_{,xx}(l) = M(l) = 0 \tag{9}$$
$$u_{,xxx}(l) = F(l) = 0 \tag{10}$$

where the forcing function is

$$f(x) = 2\mu \left[\left(\frac{t_i - |u(x)|}{t_i} \right)^{\alpha-1} + \left(\frac{t_i - |u(x)|}{t_i} \right)^{-\alpha-1} \right] u(x) \left\{ 1 - \gamma_T \sin^2 \left[\tan^{-1}(u_{,x}(x)) \right] \right\} \tag{11}$$

We denote Equation 11 as "ogden_constrained_true". Such equation can be reformulated and solved using nonlinear finite element method (FEM) with load stepping. The derivation for FEM equations is beyond the scope of this report.

The choice of Ogden hyperelastic model is not unwarranted. Many articles, such as [2], have shown that Ogden model outperforms other commonly used hyperelastic models, such as Mooney-Rivilin, Yeoh, Fung, and Neo-Hookean, in modeling biological materials. Since model verification needs to be performed first on PVC samples, it is necessary to verify for ourselves that one-term Ogden model can indeed capture the stress-stretch behavior of the PVC material, and outperforms other simplified forms of hyperelastic models.

For this purpose, material samples are built that roughly follows the ASTM article D575-91, which introduces testing methods for rubber properties in compression. Note that this is standard for testing rubber, which is only similar to the material we will be using. The samples are tested in a testing machine following pre-conditioning and strain rate specified by the document.

3 Experiments and Results

3.1 Image Registration and Motion Extraction

The test jig and registration algorithm are able to successfully segment the needle and different markers, and find the relative transformations between successive stage frames $\{S\}$'s. The voxel size of the cone-beam CT is $0.49 \times 0.49 \times 0.49\text{mm}^3$. The average registration error for the gel markers is 0.35mm, and the average error for stage markers is 0.16mm. The error for the gel markers is slightly higher, possibly due to the fact that the markers are embedded on the acryclic box, which is laser cutted; the assembly process might have introduced some error that deviates the actual marker positions from those set in the design. Nonetheless, the errors are smaller than what the CT could detect.

For the baseline scan, since the rotary stage is passive, and slight rotational deviation might occur due to the initial insertion, i.e. there could be a small rotation in the stage $z-$axis. This is indeed the case, for the detected baseline rotation typically has rotation axis $[0.206, 0.205, 0.957]$ with rotation magnitude of $0.559°$, which indeed corresponds to a small rotation in the $z-$axis. This also proves that the algorithm can pick up the rotation of the needle holder stage, and the small nonzero initial rotation can be ignored.

Due to the voxel nature of the CT scans, it is unclear where exactly the needle tip is below the threshold resolution; in addition, although different types of curves can be fitted to provide an "analytical" description of the needle shape, no single type of function can fit all deflected needle shapes. Therefore, a straightforward linear interpolation between each successive voxel occupied by the needle is used to respect the information provided by the CT without making additional assumptions.

The iterative closest point (ICP) algorithm frequntly gets stuck at local minima, possibly due to the fact that very sparse particles are used (7 for stage, 6 for gel). Therefore, an additional layer of iterative method is used with the ICP algorithm to provide consistent rigid registration to all images. The algorithm is presented in Algorithm 2. This way, the final transformation formed by $[R, t]$ will bring the source to target with one step.

Algorithm 2 Modified ICP to find rigid transformation $[R, t]$

$err \leftarrow 100$ ▷ initialize error
$R \leftarrow I_{3\times3}$ ▷ initialize rotation
$t \leftarrow [0, 0, 0]^T$ ▷ initialize translation
while $err \geq err\_threshold$ **do**
  $[R\_inc, t\_inc] \leftarrow icp(source, target)$ ▷ run ICP algorithm
  $R \leftarrow R\_inc \cdot R$
  $t \leftarrow t\_inc + R\_inc \cdot t$
  $Markers \leftarrow FT(R\_inc \cdot Markers + t\_inc)$
  if $err \geq err\_threshold$ **then** ▷ if stuck at local minimum, apply some random rotation
    $R \leftarrow Rotz \cdot R$
    $t \leftarrow Rotz \cdot t$
    $Markers \leftarrow FT(Rotz \cdot Markers)$
  end if
end while

The baseline scan will produce Nel and t_0, which are the number of finite elements needed and the translation between the two frames $\{G\}$ and $\{S_0\}$. The number of finite elements is proportional to the detected needle length in order to ensure consistent mesh size between different insertion lengths. Subsequent scans with Nel and t_0 being the input will output motion parameters necessary to run the FEM algorithm, for example, the separation between needle exit and point of insertion s_b, the lateral translation d_b, and a set of discrete needle points consistent with the number of elements.

3.2 Sample Fabrication and Testing, and Model Evaluation

As mentioned before, material samples are made and tested in a compression testing machine to confirm our assumption that one-term Ogden can indeed model the type of PVC material we'll be using for FEM model varification. Steps to produce fairly consistent sample are detailed in Appendix A. Each sample takes roughly an hour to make from start to finish, and the method is rather consistent, irregular samples is a common occurance, which makes sample fabrication a rather time-consuming process.

A total of nine samples with 100% liquid plastisol, and they are compressed with the MTS testing machine in the Department of Material Science and Engineering. The compression testing setup are shown in Figure 4a. Two pieces of sandpaper are put between the sample and the compression platens to prevent the samples sticking to the platens. An RGBD camera and a checker board pattern are introduced to the scene in order to capture the true cross-sectional area of the sample during the compression process, allowing the calculation of true stress instead of engineering stress. However, correlating compression reading with camera footage is nontrivial, and efforts are being made to sync the two sources of data.

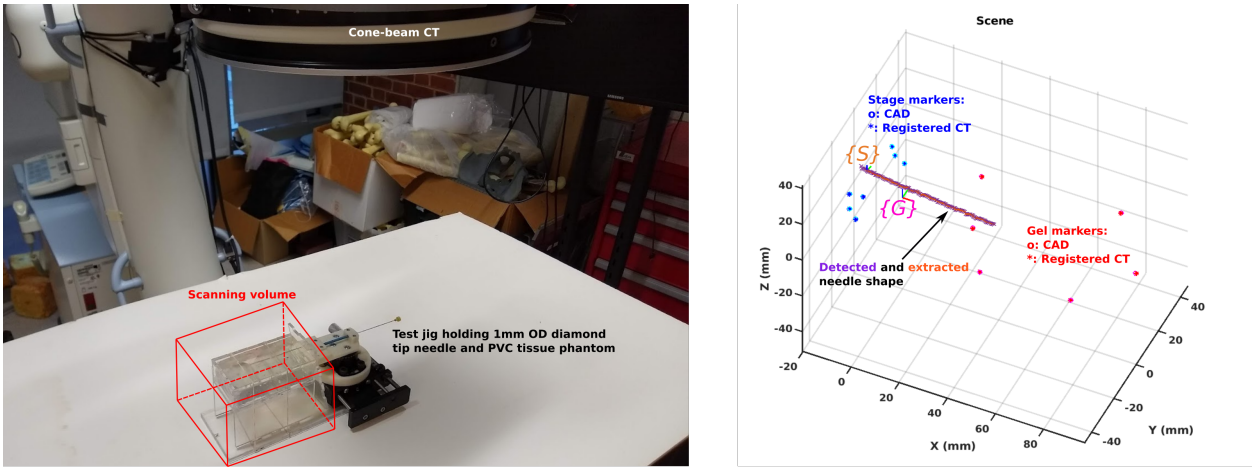

Figure 3: Image registration and motion detection with CT.

Four out of the nine curves show consistent stress-stretch behavior, and are used to fit commonly used hyperelastic material models. The purpose of which is two-fold. First, it is necessary to see which of these material models can best describe the PVC material so as to incorporate into the needle-tissue interaction model. Second, to provide some ground truth for the material parameters.

As shown in Figure 4b, one-term Ogden, Mooney-Rivlin, and two-term Yeoh models could capture the behavior very well, and are consistent between each other; Neo-Hookean model is able to capture small-stretch behavior reasonably well, but it deviates from others, and the curves, at larger stretch regions, and is rejected as a candidate hyperelastic model. The other three models all show R^2 values above 0.99, whith one-term Ogden model slightly outperforms the other two with $R^2 = 0.9943$. The three models estimated the material shear modulus to be around 13kPa. Although they are all good candidates, the one-term Ogden model is chosen, as shown in Equation 11. However, a slight variation was implemented such that the tangent modulus corresponds to engineering stress instead of true stress, and unconstrained compression instead of constrained compression, since we only have engineering stress values at the current stage. As a result, the form of Equation 11 is slightly different. The new $f(x)$, denoted as "ogden_unconstrained_eng", is presented as

$$f(x) = \frac{2\mu}{\alpha}\left[(\alpha-1)\left(\frac{t_i - |u(x)|}{t_i}\right)^{\alpha-2} + \left(1+\frac{\alpha}{2}\right)\left(\frac{t_i - |u(x)|}{t_i}\right)^{-\frac{\alpha}{2}-2}\right] u(x)\left\{1-\gamma_T \sin^2\left[\tan^{-1}(u_{,x}(x))\right]\right\} \tag{12}$$

With the setup shown in Figure 3 and a block of sample with the liquid PVC, verification of the proposed needle-tissue interaction model is carried out in the following format:

- Needle: 1mm outer diameter diamond tip needle
- Insertion depths: ∼20mm, ∼40mm, ∼60mm
- Linear stage displacements: 0mm to 10mm back to 0mm with 2.5mm increments

The simulation resutls are shown in Table 1. The quantity d_b is the detected needle base lateral displacement. Note that this is different from the linear stage motion, since the passive stage naturally rotate due to interaction between needle and PVC, and therefore the actual lateral displacement at the needle base is smaller than that of the linear stage. Using element size of approximately 0.5mm, the number of elements is approximately twice the insertion length, and the averaged error across all elements is below 0.1mm. The error at the needle tip is also shown in the table. The error is generally larger for larger displacements. For most cases, the errors are under the resolution threshold of the CT.

Another round of experiment is done with porcine muscles purchased from local grocery store. According to [3], the one-term Ogden parameters of porcine muscles are similar to those of the human gastrocnemius

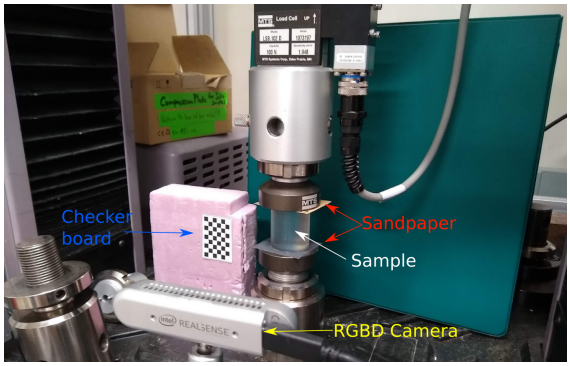

(a) Material samples being compressed in the MTS testing machine. Two pieces of sandpaper are used to prevent sample sticking to the compression platens.

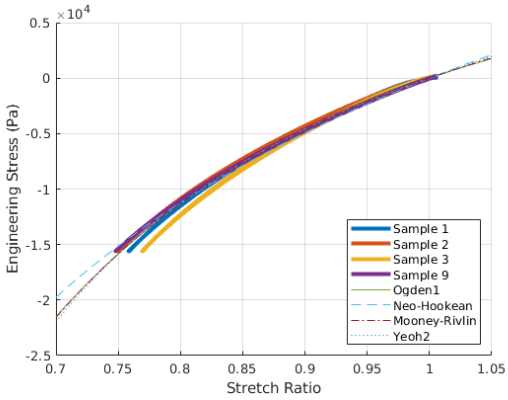

(b) Four consistent stress-stretch curves fitted with hyperelastic material models: one-term Ogden, Neo-Hookean, Mooney-Rivlin, and two-term Yeoh.

Figure 4: Sample testing and curve fitting.

Table 1: PVC Simulation Result

20mm			40mm			60mm		
d_b	Avg. El. Err	Tip Err	d_b	Avg. El. Err	Tip Err	d_b	Avg. El. Err	Tip Err
0.91	0.02	0.35	0.94	0.03	0.54	0.96	0.02	0.46
2.05	0.02	0.14	2.08	0.04	0.40	1.59	0.02	0.58
3.08	0.02	0.39	3.07	0.04	0.68	2.00	0.02	0.23
4.07	0.02	0.14	4.12	0.04	1.01	2.96	0.02	0.36
3.10	0.02	0.32	3.10	0.04	0.74	4.02	0.03	0.60
2.05	0.02	0.02	2.11	0.03	0.41	3.02	0.02	0.27
1.07	0.02	0.21	1.07	0.02	0.59	2.06	0.02	0.50

regardless of fiber orientation. The authors reported average material properties of $\mu = 3.63$kPa and $\alpha = 8.74$ for their porcine samples, and $\mu = 3.43$kPa and $\alpha = 8.74$ for their human muscle samples. Since the numbers the authors reported are based on true stress measure, therefore, Equation 11 is used, along with the reported value for porcine muscle.

The procedure is similar to that described before, but restricting only to the "forward" displacement path from 0mm to 10mm without going backwards. The setup is shown in Figure 5, and the results are summarized in Table 2. The errors at the tip are consistently below the resolution threshold of CT.

4 Discussion

From the results shown in Section 3, it appears that the proposed needle-tissue interaction model, along with the nonlinear FEM solution, can predict the needle bending behavior to great accuracy, provided

Table 2: Porcine Simulation Result

20mm			40mm			60mm		
d_b	Avg. El. Err	Tip Err	d_b	Avg. El. Err	Tip Err	d_b	Avg. El. Err	Tip Err
0.85	0.03	0.37	0.96	0.01	0.03	1.21	0.02	0.04
1.63	0.02	0.34	1.99	0.02	0.06	2.29	0.02	0.04
2.40	0.02	0.37	3.01	0.02	0.06	3.37	0.02	0.14
3.22	0.02	0.18	4.05	0.02	0.01	4.45	0.02	0.30

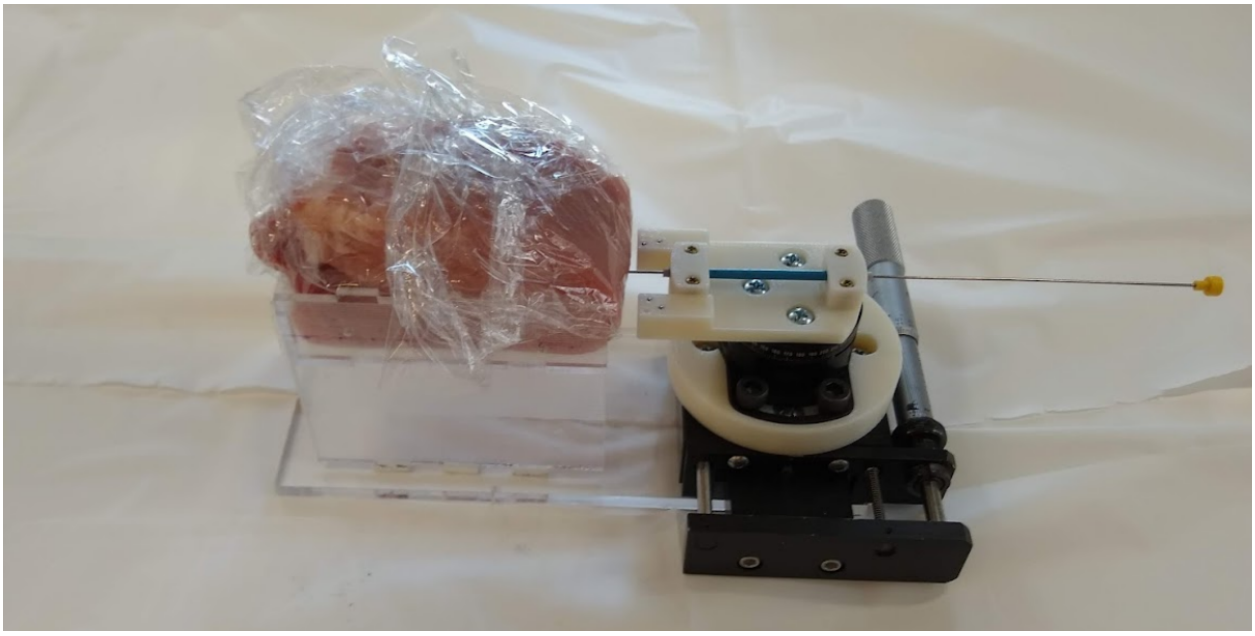

Figure 5: Porcine sample cut and fitted on the test jig. The sample is wrapped in a piece of kitchen plastic wrap for sanitary concerns. The needle is inserted from the side with rather uniform muscle composition.

that the needle base deflection is small (in this case, less than 5mm) and there are tissue parameters in biomechanic literatures. As shown in [4], such numbers are prevelant in biomechanical research, and more accurate models can be expected as experimental methodologies improve.

The needle-tissue interaction model, along with the use of nonlinear material hyperelastic model, relies on an important fact that the initial length of the tissue is known. This is crucial in determining where exactly on the stress-stretch curve does the current displacement lies. It is not a limiting factor in the current study, since the material is constrained in a container with known size; however, for some clinical scenarios where the needle is inserted into a large muscle, such as in lumbar injection, this initial tissue length is difficult to determine.

It is of great interest to further investigate the validity of the proposed needle-tissue interaction model under larger needle base displacement, and in turn larger tissue deformation. However, the underlying assumption for this research is the required needle tip adjustment is small; and if large adjustment is needed, the needle could be retracted to a shallower depth to make small adjustment in order to correct subsequent needle path. Nonetheless, for the sake of testing the valid range of tissue deformation this model can reliably capture, such test is necessary.

More tests can also be performed on other tissue samples, in addition to multi-layer samples as well, such as porcine sample with skin, fat, and muscle. The implementation of a lookup table for tissue properties in the FEM routine allows such multi-layer media to be simulated.

With such encounraging results, a necessary next step is to re-formulate the problem into a boundary control problem, where instead of a static boundary condition formulation, the boundary values are treated as control inputs where the inputs vary with time. Such problem is prevelant in the control of long beam-like structures subject to external force as to control the resulting vabriation [1]. However, since most boundary control literature deal with control efforts at the end of the beam with fixed displacement, while in this case the controls are beam displacement and slope, a direct application of the literature solution is not readily possible.

References

[1] Jiang, T., J. Liu, and W. He (2018). Boundary control for a flexible manipulator with a robust state observer. *Journal of Vibration and Control 24*(2), 260–271.

[2] Mihai, L. A., L. Chin, P. A. Janmey, and A. Goriely (2015, Sep). A comparison of hyperelastic constitutive models applicable to brain and fat tissues. *Journal of The Royal Society Interface 12*(110), 20150486.

[3] Mo, F., Z. Zheng, H. Zhang, G. Li, Z. Yang, and D. Sun (2020). In vitro compressive properties of skeletal muscles and inverse finite element analysis: Comparison of human versus animals. *Journal of Biomechanics 109*, 109916.

[4] Singh, G. and A. Chanda (2021, oct). Mechanical properties of whole-body soft human tissues: a review. *Biomedical Materials 16*(6), 062004.

[5] Wang, Y., G. Li, K.-W. Kwok, K. Cleary, R. H. Taylor, and I. Iordachita (2021). Towards safe in situ needle manipulation for robot assisted lumbar injection in interventional mri. In *2021 IEEE/RSJ International Conference on Intelligent Robots and Systems (IROS)*, pp. 1835–1842.

Figure 6: Plunger (left) and tube (right) used to create samples. The detachable bottom plate (black dotted) can be attached to either end of the tube. The taped end is slightly looser than the non-taped end. The tighter end is for forming the overall shape and a uniform bottom surface, while the looser end is used to remelt top portion of the sample in order to create a uniform top surface. The plunger is used to push the sample out of the tube, and to apply pressure during the remelting step.

Appendices

A Material Sample Fabrication

This following instruction is for making samples from 100% liquid PVC from 142 Super Soft/Low Odor/Ultra Clear plastisol from Bait Plastics (link to product page). The procedure needs to be performed in a fume hood with proper personal protection equipment. Refer to Figure 6.

1. Pre-heat the stove to 325°C
2. Measure 50ml liquid
3. Put bottom plate to the tighter end of the tube
4. Pour liquid in the tube and heat for 30mins, and shake the tube at 15min time stamp
5. With gloves on, transfer tube into a liquid bath that submerges the bottom section of the tube, and let it sit for 15 mins
6. Take the tube out of the bath. The bottom section should be cool, while the top section might still be warm
7. Remove the bottom plate by pulling straight. Do not twist and turn the bottom plate, for the sample surface would be destroyed
8. Use your finger to peel the wall of the sample off of the inner wall of the tube. Apply lubricants to the surface boundary to assist this peeling process
9. If the sample does not come off, align the plunger to the opening and let it slide slowly until it touches the other end of the sample. Do not force the plunger in, for it will force air into the sample and damage the sample
10. Slowly push the plunger until the sample comes out at the other end
11. Put the sample sideways on a clean working surface. With a sharp blade, carefully cut the non-flat side to a desired length for remelting. Try to make a flat cut, as this will improve the remelted surface

12. Reheat only the bottom plate to 300°C
13. Apply lubricant to the inner wall of the taped side of tube, and insert the sample flat-side-in, with rough surface facing outward
14. Use plunger to generate air pressure to position the sample to the desired location. Take out the plunger
15. Put on gloves, and use a plier to transfer the hot bottom plate to a workbench, and quickly attach the tube to the bottom plate. Once attached, use the plunger and a free weight to apply pressure from the other end. Let it sit for 2mins
16. Transfer everything back to the liquid bath, and wait for 10mins
17. Take everything out of liquid bath, and remove bottom plate. Process complete

B Management Summary

B.1 Who Did What

I did all the above work, but I would like to thank Lydia Al-Zogbi for her assistance in PVC sample fabrication and testing, as well as kindly providing the liquid PVC she purchased.

B.2 Accomplished vs Planned

Most of the project went as originally planned. A shift in research focus occured towards the end of this project, where the model verification step is extended beyond just PVC samples, but to some animal tissue as well.

B.3 What Might Be Next

Trajectory optimization and path planning are pushed back indefinitely due to the complexity of the problem as well as limited time to properly formulate these problems; efforts will be made in the Summer to address such issue.

B.4 What I Learned

It is utterly important to have the correct tools in order to achieve satisfactory results. Strenuous effort was put into sample fabrication, especially figuring out what tools are needed in order to 1) contain the PVC liquid, 2) sustain a temperature ≥ 300°C 3) eliminate uneven surfaces of the produced samples. After understanding the list of requirements, I was extremely lucky in finding exactly what I needed in the trash bin of the LCSR machine shop: an 1.125in (which matches exactly what the ASTM standard specifies) ID cylindrical tube with a matching bottom plate, along with a cylinder with just the right OD to form a close-to-airtight seal with the tube. The two ends of the tube have slightly different fit with the bottom plate, with one end fits slightly tighter than the other, which is exactly what I had hoped in order to remelt the sample top surface in order to bring it even.

If such apparatus were not available, I do not think this project would progress as well as it did.